Phase I Trial of the Positron-Emitting Arg-Gly-Asp (RGD) Peptide Radioligand ^{18}F-AH111585 in Breast Cancer Patients

Laura M. Kenny[1], R. Charles Coombes[1], Inger Oulie[2], Kaiyumars B. Contractor[1], Matthew Miller[2], Terence J. Spinks[3], Brian McParland[2], Pamela S. Cohen[2], Ai-Min Hui[2], Carlo Palmieri[1], Safiye Osman[2], Matthias Glaser[2], David Turton[2], Adil Al-Nahhas[3], and Eric O. Aboagye[1]

[1]Department of Oncology, Imperial College Faculty of Medicine, Hammersmith Hospital, London, United Kingdom; [2]GE Healthcare Medical Diagnostics, Amersham Place, Buckinghamshire, United Kingdom; and [3]Department of Nuclear Medicine, Imperial College Faculty of Medicine, Hammersmith Hospital, London, United Kingdom

The integrin $\alpha_v\beta_3$ receptor is upregulated on tumor cells and endothelium and plays important roles in angiogenesis and metastasis. Arg-Gly-Asp (RGD) peptide ligands have high affinity for these integrins and can be radiolabeled for PET imaging of angiogenesis or tumor development. We have assessed the safety, stability, and tumor distribution kinetics of a novel radiolabeled RGD-based integrin peptide-polymer conjugate, ^{18}F-AH111585, and its feasibility to detect tumors in metastatic breast cancer patients using PET. **Methods:** The biodistribution of ^{18}F-AH111585 was assessed in 18 tumor lesions from 7 patients with metastatic breast cancer by PET, and the PET data were compared with CT results. The metabolic stability of ^{18}F-AH111585 was assessed by chromatography of plasma samples. Regions of interest (ROIs) defined over tumor and normal tissues of the PET images were used to determine the kinetics of radioligand binding in tissues. **Results:** The radiopharmaceutical and PET procedures were well tolerated in all patients. All 18 tumors detected by CT were visible on the ^{18}F-AH111585 PET images, either as distinct increases in uptake compared with the surrounding normal tissue or, in the case of liver metastases, as regions of deficit uptake because of the high background activity in normal liver tissue. ^{18}F-AH111585 was either homogeneously distributed in the tumors or appeared within the tumor rim, consistent with the pattern of viable peripheral tumor and central necrosis often seen in association with angiogenesis. Increased uptake compared with background ($P = 0.002$) was demonstrated in metastases in lung, pleura, bone, lymph node, and primary tumor. **Conclusion:** ^{18}F-AH111585 designed to bind the $\alpha_v\beta_3$ integrin is safe, metabolically stable, and retained in tumor tissues and detects breast cancer lesions by PET in most anatomic sites.

Key Words: integrin; RGD; tumor; positron emission tomography; $\alpha_v\beta_3$

Angiogenesis, invasion, and metastasis are important hallmarks of cancer (*1*). These processes are regulated in part by cell-adhesion receptors. Integrins are a family of cell-adhesion receptors that facilitate the interaction of tumor cells and tumor endothelial cells with the extracellular matrix (*2,3*). The integrin $\alpha_v\beta_3$ receptor is expressed at low levels on epithelial and mature endothelial cells but is upregulated on tumor cells and tumor endothelial cells of varying tumor types, including breast cancer (*2,4–8*), making it a valuable tumor-diagnosing tool. Furthermore, Gasparini et al. have demonstrated an association between expression of $\alpha_v\beta_3$ and relapse-free survival in both node-positive and node-negative breast cancer (*6*), suggesting the potential prognostic value of imaging of such receptors. The tripeptide Arg-Gly-Asp (RGD) amino acid sequence is present in several extracellular matrix proteins including vitronectin, fibronectin, and thrombospondin. Peptide ligands containing RGD have high affinity for these integrins and, when labeled appropriately with positron- or γ-emitting radioisotopes, can be used for imaging $\alpha_v\beta_3$ receptor levels by PET or SPECT (*9,10*). For instance, the uptake of the glycosylated cyclic pentapeptide ^{18}F-galacto-RGD in a variety of patient tumors, including breast cancer, was associated with $\alpha_v\beta_3$ expression detected on the imaged tumor material when excised and examined by immunohistochemistry (*9,10*). These radioligands may have value for monitoring antiangiogenic therapeutics, the development (selection of optimal dose and assessment of clinical response) of which can pose a substantial challenge.

These promising reports have created an interest in the imaging field to develop novel integrin imaging agents. In this article, we present a clinical study of a new cyclic RGD-based radioligand for $\alpha_v\beta_3$, ^{18}F-AH111585, the core sequence of which was originally discovered from a phage display library (as ACDCRGDCFCG) (*11*). Because most peptides are rapidly degraded *in vivo* and have a short plasma half-life, optimization of the original peptide sequence to

AH111585 included, among other things, the cyclization and introduction of multiple disulphide bridges to stabilize the molecule with minimal disruption of the RGD pharmacophore (12). Furthermore, introduction of a polyethylene glycol-like spacer at the C terminus was designed to further stabilize the peptide against carboxypeptidases and increase the circulation life span, thereby increasing tumor retention (12). The binding affinities (IC$_{50}$) of ^{19}F-AH111585 to $\alpha_v\beta_3$, $\alpha_v\beta_5$, and $\alpha_{iib}\beta_3$ were 11.1, 0.1, and 281 nM; corresponding values for positive-control echistatin were 2.0, 3.9, and 1.2 nM, indicating that the product had retained selective binding affinity to the receptors. We have evaluated several of these design goals for ^{18}F-AH111585, including stability and preliminary diagnostic value in the clinical studies reported here. Furthermore, we have determined the kinetics of radioligand–tissue interactions to objectively inform the appropriate time for imaging in a larger patient population. Dynamic imaging studies and associated description of the kinetics of radioligand interaction with receptors in human breast tumors are reported.

MATERIALS AND METHODS

Study Design and Clinicopathologic Features

The aims of this study were to determine the safety, stability, preliminary diagnostic value, and tissue distribution kinetics of the novel $\alpha_v\beta_3$ radioligand ^{18}F-AH111585. The Hammersmith Hospitals NHS Trust Research Ethics Committee granted ethical approval for the study. The Medicines and Healthcare Products Regulatory Agency, United Kingdom, approved the use of an investigational medicinal product (IMP) (^{18}F-AH111585). The administration of the radiopharmaceutical was approved by the Administration of Radioactive Substance Advisory Committee, United Kingdom. The inclusion criteria included having American Joint Committee on Cancer–stage IV breast cancer; being more than 25 y old; having an Eastern Cooperative Oncology Group (ECOG) performance status of 0–2 (13); being postmenopausal, surgically sterile, or posthysterectomy or having a negative pregnancy test on the day of the scan; and having at least 1 lesion greater than 1 cm that had not been previously irradiated. The

exclusion criteria included receiving chemotherapy within the 3 wk before scanning; having received an IMP within 30 d before the scan or being due to receive an IMP within 24 h; and undergoing occupational monitoring for radiation exposure. The patient demographics are shown in Table 1. For patients who had had a CT scan within 4 wk of the PET scan, the 2 datasets were compared. Comparison of PET with CT was performed by masked assessment because the primary aim was safety, and only a preliminary diagnostic value was sought. The CT scans were done on a 16-row spiral CT scanner (Siemens).

Radiosynthesis of ^{18}F-AH111585

The chemical synthesis of the precursor for ^{18}F-AH111585 has previously been described (12). Radiosynthesis was performed at Hammersmith Imanet on an automated module (TRACERlab FX $_{F-N}$; GE Healthcare) by coupling an aminooxy-functionalized precursor of ^{18}F-AH111585 with 4-^{18}F-fluorobenzaldehyde at pH 3.5 to form the oxime ^{18}F-AH111585. A full description of the synthesis has been published elsewhere (14). The specific activity of the injectate, determined by high-performance liquid chromatography (HPLC), ranged between 76 and 170 GBq/μmol.

PET

All scans were performed on a scanner (ECAT962/HR+; Siemens) that had a 15.5-cm axial field of view (transaxial, 58 cm). Before injection of the radioligand, the tumor of interest was centered in the field of view, and a transmission scan was performed using rotating ^{68}Ge sources for attenuation correction. All patients were administered a single-bolus intravenous injection of ^{18}F-AH111585, with doses ranging between 198.8 and 292.1 MBq. Scanning was performed dynamically in 3-dimensional mode in a single bed position for 61.5 min with 32 discrete time frames (30 s × 1 [background frame]; 10 s × 6; 15 s × 4; 30 s × 4; 120 s × 6; 180 s × 5; 600 s × 3). Data were Fourier rebinned into 2-dimensional slices and reconstructed (with correction for attenuation, scatter, and dead time) using filtered backprojection (ramp filter kernel full width at half maximum of 2.0 mm, 128 × 128 voxels of 2.62 × 2.62 mm^2, and slice thickness of 2.42 mm). The measured in-plane image resolution (transaxial) was 8.5 mm in full width at half maximum, and the axial image resolution was 5.0 mm. Region-of-interest (ROI) definition was performed by manually tracing the outline of lesions (whole or portions—outer

TABLE 1
Patient Demographics

Patient no.	Site of disease	Time from original diagnosis (y)	Primary removed	No. of previous chemotherapy regimes	Previous endocrine treatment	Histology
1	SCF	7	Y	5	Y	Grade 2 IDC, ER 210/300, PR 60/300, cerbB2 –ve
2	Breast, bone	1	N	0	Y	Grade 2 IDC, ER 300/300, PR 120/300, cerbB2 –ve
3	Liver, bone	2	Y	2	Y	Grade 2 IDC, ER 300/300, PR 300/300, cerbB2 –ve
4	Liver	8	Y	1	Y	Grade 2 IDC, ER 300/300, PR 210/300, cerbB2 –ve
5	Lung	2	Y	4	N	Grade 3 IDC, ER –ve, PR –ve, cerbB2 –ve
6	Pleura, lung, lymph nodes	9	Y	2	Y	Grade 2 IDC, ER 210/300, PR –ve, cerbB2 –ve
7	Liver, pleural fluid	8	Y	1	Y	Grade 2 IDC, ER 220/300, PR 60/300, cerbB2 –ve

IDC = invasive ductal carcinoma; ER = estrogen receptor; PR = progesterone receptor; –ve = negative.

and necrotic core) on multiple slices, or in the case of muscle and normal breast, lung, and liver tissues by drawing similar-sized regions on multiple slices of the image. Image analysis was carried out using analysis software (Analyze Version 7; Biomedical Imaging Resource) as previously reported (15) to obtain time–activity curves.

Blood Sampling and Metabolite Analysis

Blood samples were taken via a radial artery cannula continuously for the first 10 min during scanning; discrete samples (5–10 mL) were taken at 5, 10, 15, 30, and 60 min after injection. The discrete blood samples (1-mL aliquots of total blood and plasma) were analyzed for total activity using a sodium iodide well counter to determine the plasma-to-blood activity ratio. ^{18}F-AH111585 parent fraction and metabolites were determined in the discrete samples by reversed-phase HPLC with radiochemical detection (radio-HPLC). For this, aliquots (~7 mL) of blood were centrifuged at 3,000g for 1 min at room temperature to obtain plasma. The resulting plasma was passed through a 0.22-μm filter and the volume recorded. A 100-μL aliquot was counted for total activity on a γ-counter. The remainder was loaded onto an online C18 cartridge connected to an HPLC system and washed with 13.5 mL of $(NH_4)_2HPO_4$. The activity in two 5-mL aliquots of the wash was determined. The activity remaining on the C18 cartridge was backwashed onto a C18 HPLC column (Gemini; Phenomenex) (250×10 mm; 10 μm) and eluted with a mobile phase comprising 55% v/v methanol/0.01 M KH_2PO_4, pH 4, running at a flow rate of 3 mL/min for 20 min and detected by dual UV–radioactivity detection (210 nm). The HPLC eluates were collected, total volume was recorded, and aliquots (2×5 mL) were counted. All data were decay-corrected to the start of injection. Peak areas for ^{18}F-AH111585 on the chromatograms were analyzed and expressed as a ratio to total activity in the original plasma samples. For modeling purposes, a correction for loss of parent ^{18}F-AH111585 on the online C18 cartridge was made by fitting the parent plasma curve to a straight line to derive a slope and an intercept. These parameters were then used to scale the data such that the y-intercept was 1. The analysis was performed using a plotting tool (MATLAB version 6; The Mathworks). Both total arterial plasma and parent plasma input functions were derived from these analyses to aid mathematic modeling of tissue data.

Kinetic Analysis of Tumor and Normal Tissue Radioactivity

A key aspect of this—to our knowledge—first human study was to define the tissue kinetic profile of ^{18}F-AH111585 and to determine kinetic parameters that describe the retention of the radioligand. Both semiquantitative and fully quantitative parameters were calculated. Curves of tissue activity (kBq/mL) versus time were decay-corrected and normalized for injected activity (kBq) and body surface area ([BSA] in m²; $0.20247 \times \text{height(m)}^{0.725} \times \text{weight(kg)}^{0.425}$) or body weight ([BW] in kg) to obtain standardized uptake value (SUV), standardized uptake value with body surface area normalization (SUV_{BSA}) (m²/mL), and standardized uptake value with body weight normalization (SUV_{BW}) (kg/mL), as previously described (15). The rate constant, K_i, for the net-irreversible retention of the radioligand within the imaging time was calculated as previously described (15,16) by the modified Patlak graphical method (Ki_{mod}) (assuming that the metabolites do not bind to the receptor) or the classic Patlak graphical method (Ki_{class}) (with total plasma input function, assuming that the

metabolites do bind to the receptor). We also assessed the fractional retention of the radioligand (FRT) and the mean residence time (MRT) by a general deconvolution technique, spectral analysis (15,17). FRT was calculated as the ratio of the unit impulse response function at 56.5 min to that at 1 min (14).

Safety Monitoring

Safety data were collected after administration of ^{18}F-AH111585 and throughout the follow-up period of 24 h for every patient. Safety monitoring included the recording of adverse events, changes in vital signs, physical examination, electrocardiogram (ECG), and laboratory parameters (serum biochemistry, hematology, coagulation, and urine analysis). Blood samples were obtained at baseline, 30 min, 150 min, and 24 h after radioligand administration and analyzed by a central laboratory; patients were followed further if abnormalities were detected. A standard 12-lead ECG was obtained at various preadministration and postadministration time points, from 5 min before administration to up to 24 h after administration. In addition, the lead II ECG was continually monitored from 5 min before administration until 15 min after administration.

Statistics

Data for individual tumors and tissues, as well as summary data, were reported. A 2-tailed Wilcoxon matched-pairs test was used to compare the uptake and kinetic parameters in tumor lesions with corresponding normal tissues. A P value of more than 0.05 was considered significant. Graphics software (GraphPad Prism version 3.0; GraphPad Software) was used to perform the analysis.

RESULTS

Dose Administered

The mean administered activity was 232.5 ± 37.6 MBq (range, 198.8–292.3 MBq), and the mean administered mass dose was 3.9 ± 1.2 μg (range, 3.0–6.0 μg).

Safety

Administration of ^{18}F-AH111585 was well tolerated by all 7 patients. No drug-related adverse events were reported for patients in this study. No clinically important trends indicative of a safety signal were noted for laboratory parameters, vital signs, or ECG parameters. Transient, asymptomatic increases in activated partial thromboplastin time (APTT) after ^{18}F-AH111585 injection were observed in all 7 patients (5.3–31.6 s above baseline and up to 30.6 s above normal), which were completely reversible by 48 h. The transient increases in APTT were likely due to the use of intravenous heparin flushes in the same catheter from which the APTT samples were drawn. There was no clinical bleeding, and none of the patients had a history of underlying bleeding dyscrasias.
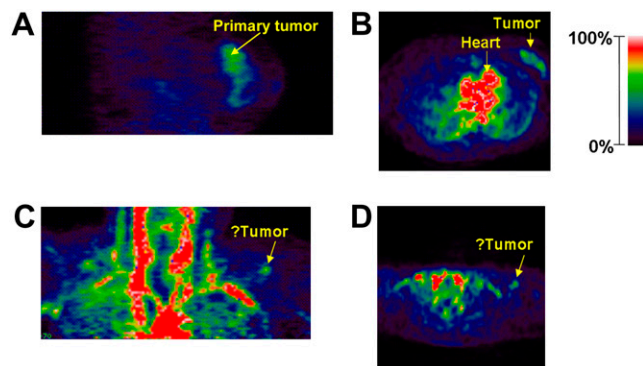
Preliminary Diagnostic Value of ^{18}F-AH111585

Seven patients with metastatic breast cancer lesions were enrolled in the study. A total of 18 tumor lesions were visualized on CT. Three patients presented with metastases only in the liver, 2 with metastases only in the lung, and 1 with metastases only in bone. One patient presented with metastases in bone and a supraclavicular lymph node. None
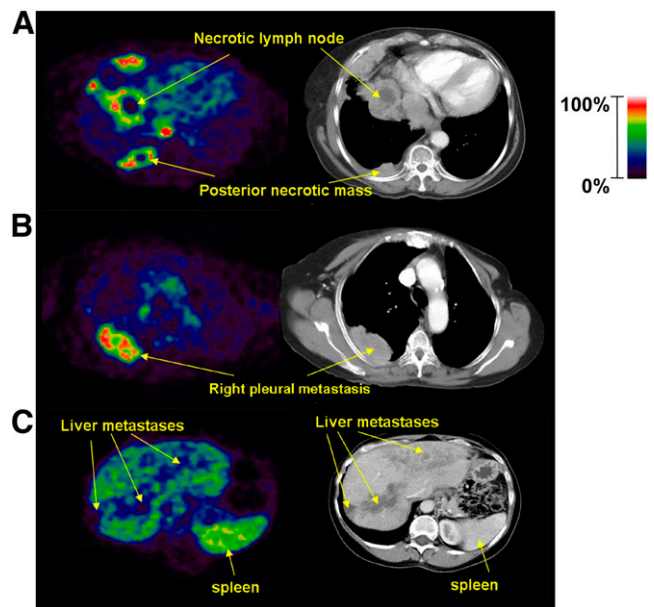
of the patients had brain metastases. Of the 18 tumors detected by CT, all were visible on ^{18}F-AH111585 PET. Tumors in regions of low background activity—for example, primary breast (Figs. 1A and 1B) and lung metastases (Figs. 2A and 2B)—were clearly identifiable as hyperintense foci on PET. Two lung metastases showed the highest uptake. ^{18}F-AH111585 was either homogeneously distributed in these tumors or appeared within the tumor rim. Tumors in regions of high background activity, for example, liver metastases (Fig. 2C), were identified as hypointense foci. In 1 patient with liver metastatic lesions, PET detected 8 lesions but CT detected 7; the additional lesion on PET might be considered as a false-positive. In 1 patient with a clinically suggestive supraclavicular fossa lymph node (SCF) (clearly palpable mass) not visualized on CT, it was difficult to establish whether a hyperintense region detectable on PET was indeed a tumor (Figs. 1C and 1D), because the CT scan data were inconclusive and this lymph node was not biopsied. For bone metastatic tumors, bone scintigraphy was used as a standard reference. The tumors seen on the PET scan (narrower field of view) were matched with those on the bone scan; however, complete correlation of lesions on the bone scan with the PET scan was not possible because whole-body PET was not performed.

Stability of ^{18}F-AH111585

^{18}F-AH111585 was stable after intravenous injection to patients (Fig. 3). Parent activity eluted at a retention time of approximately 17.5 min (Figs. 3A and 3B). The radioligand was slowly metabolized to hydrophilic metabolites that eluted between 10 and 15 min on the chromatogram. A summary of the proportion of parent-to-total activity is shown in Figure 3C. The mean ($\pm$SEM; 7 patients) percentage of parent radioligand in plasma at 60 min after injection of ^{18}F-AH111585 was 74.48 ± 3.18.

FIGURE 1. PET images showing localization of ^{18}F-AH111585 in patient 2 with grade II invasive ductal breast carcinoma in sagittal (A) and transverse (B) views. PET images of patient 1 with SCF in coronal (C) and transverse (D) views. See also color bar for PET images.
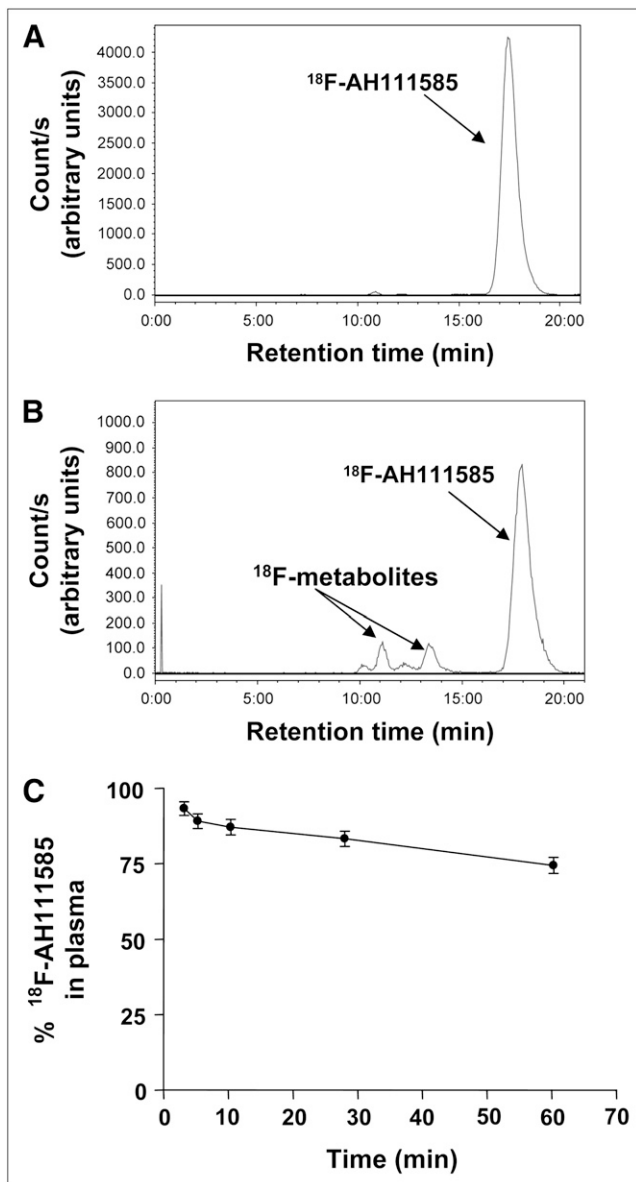

FIGURE 2. ^{18}F-AH111585 PET of metastatic lesions and corresponding CT images showing increased signal in periphery of lesions in patient with lung and pleural metastases (A), intralesion heterogeneity of uptake within pleural metastasis in PET image, which was not demonstrated as necrosis on corresponding CT section (B), and liver metastases imaged as hypointense lesions because of high background signal (C). High uptake in spleen is possibly due to blood pooling. See also color bar for PET images.

Tissue Distribution Kinetics of ^{18}F-AH111585

The uptake kinetics in tumors and normal breast, lung, and liver were analyzed. The profile of ^{18}F-AH111585-derived activity in normal lung tissue was characterized by rapid delivery and rapid washout (Fig. 4A). Similarly, activity cleared rapidly from both plasma and blood with a half-life of about 10 min; the plasma-to-blood activity ratio was less than 1 at all time points (Fig. 4B). In contrast, tumor activity increased continually, reaching a plateau at about 40–60 min. There were large variations in SUVs among individuals, among different tumor types, and even between tumors of the same cancer type (in 1 patient) (Table 2). For example, in patient 5 (with 4 lung metastatic tumors), the SUV_{BW} in tumors varied from 2.0 to 40.0 g/mL (Table 2). In general, lung metastases showed the highest SUV; the primary tumor and liver metastases showed lower uptake than did the lung metastases.

Analysis of the kinetic data indicated that the radioligand was irreversibly trapped in tumors within the imaging time during the time period of evaluation (1 h). Patlak plots for a lung metastasis and corresponding normal lung tissue are shown in Figures 4C and 4D, respectively. A discernible linear phase was seen, indicating irreversible trapping; the slope, K_i, was higher in the tumor than in the normal lung (Figs. 4C and 4D). Other retention parameters, including FRT and MRT, were generally higher in tumors than in normal tissues (Table 2). Because of potential spillover effects from normal liver

FIGURE 3. Radiochromatograms of ^{18}F-AH111585-derived radioactivity in plasma, assessed at 2.5 min (A) and 60 min (B) after injection of the radioligand. Plasma samples were processed for HPLC analysis as described in "Materials and Methods." Plots are parent ^{18}F-AH111585 and metabolites, decay-corrected to start of sample injection. (C) Proportion of unmetabolized ^{18}F-AH111585 to total ^{18}F-radioactivity in plasma as function of time, measured as described in "Materials and Methods." Bars are ±SEM; $n = 7$ patients.

tissue in the case of liver metastases, statistical analyses were performed separately for liver and nonliver lesions. Similarly, there are potential errors for quantifying uptake in necrotic regions surrounded by a high-uptake tumor rim; hence, the necrotic regions were not included in the statistical analysis of tumors. Significant difference existed between tumor and normal-tissue uptake of the radioligand for SUV_{BSA}/SUV_{BW}, FRT, and MRT (nonliver lesions: SUV, $P = 0.002$, and FRT, $P = 0.0039$; liver lesions: SUV/FRT, $P = 0.0078$, and MRT, $P = 0.0391$). For Ki_{mod} and Ki_{class}, the difference was significant for nonliver lesions only ($P = 0.002$). The necrotic centers of lymph nodes in patient 6 were not included in the statistical analysis because of concern about possible spillover effects.
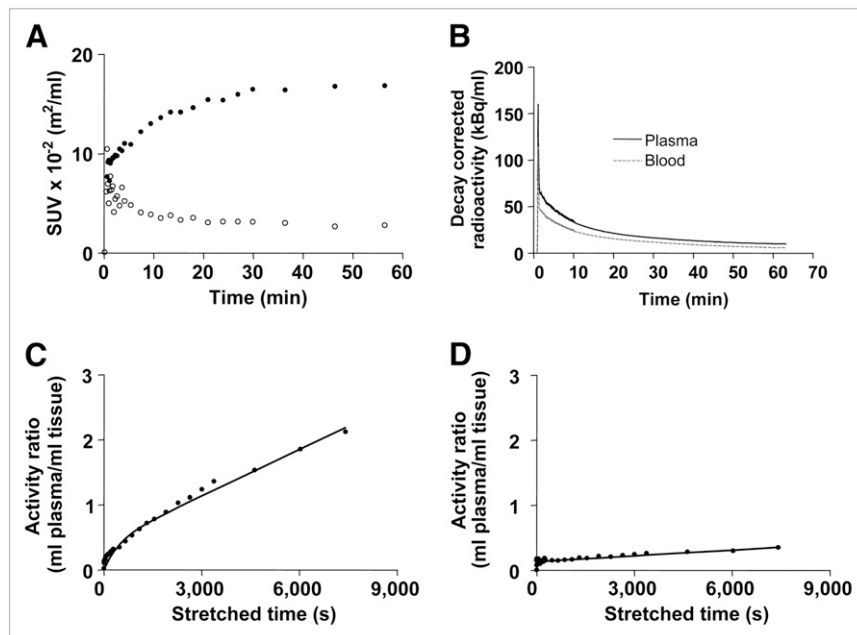
DISCUSSION

We have demonstrated for the first time, to our knowledge, that the RGD-containing radiolabeled peptide ^{18}F-AH111585 is stable *in vivo*, rapidly cleared from the blood, and retained in tumors and detects tumors by PET in breast cancer patients.

Because the integrin $\alpha_v\beta_3$ receptor is upregulated on most tumors, several RGD-based peptide ligands are being developed for imaging tumors by nuclear methods (9,10,18–22). An example is ^{18}F-galacto-RGD, whose binding correlated with receptor levels in a variety of tumors including breast cancer (9,10). Despite similarities in the RGD motif, the design strategy for ^{18}F-AH111585 (12) is distinct from ^{18}F-galacto-RGD, which was modified with a sugar amino acid to enhance systemic elimination (19). In this article, we described the—to our knowledge—first human study of a new RGD peptide, ^{18}F-AH111585, for imaging tumors in the metastatic setting. We assessed the safety, preliminary diagnostic value, *in vivo* stability, and tissue distribution kinetics of ^{18}F-AH111585 in patients.

We found ^{18}F-AH111585 PET to be safe and well tolerated, with no adverse events in the 7 patients studied. ^{18}F-AH111585 PET was able to detect all 18 tumor lesions that were identified on CT within the PET field of view. The one discrepancy was seen in a patient who had a clearly palpable lymph node visualized on the PET scan that was not conclusively seen on the CT scan. The difficulty in identifying such lesions may be due in part to the high density of vessels at the anatomic location of the suspected lesion. In general, tumors were hyperintense in several anatomic locations, including breast and lungs. The high *in vivo* stability of the radioligand together with its retention in tissue may have contributed to this finding. Although there is potential for partial-volume effects with lung metastases, all the tumors analyzed in this study were greater than 1 cm, which obviates significant partial-volume effects.

^{18}F-AH111585 was either homogeneously distributed in the tumors or appeared within the tumor rim; this finding is consistent with the general principles regarding the distribution of angiogenesis within the outer zones of breast tumors, where viable tumors exist (23–26). In contrast, tumors were hypointense in the liver. We speculate that the high liver background may be because of the densely vascularized nature of the organ and metabolism of ^{18}F-AH111585 by the liver. The demonstration of lower MRT levels in the liver than in liver metastases, despite the high ^{18}F-AH111585-derived activity levels in the former, supports this assertion. Prominent accumulation of RGD peptide ligands in the liver has been previously reported in mice and humans, which is consistent with our findings (17,27). In a separate study,

FIGURE 4. (A) Typical time vs. radioactivity curves in pleural metastasis (Fig. 2B) and lung. Data were decay-corrected and normalized to injected radioactivity and body surface area. Tumor, closed circles; lung, open circles. (B) Radioactivity in blood and plasma of same patient as in A. Terminal half-lives of blood and plasma curves were 9.30 and 10.95 min, respectively. (C) Patlak plot of tumor data from Figure 2B, showing initial exponential phase and discernible linear phase indicating net-irreversible trapping. (D) Patlak plot of lung data from Figure 2B, showing much-reduced net-irreversible trapping. Quantitative analysis of tumor data using graphical transformation in figure examples was done with total plasma input function ("Materials and Methods").

breast adenocarcinoma liver metastases appeared to have low angiogenic potential (*28*), which may contribute to the hypointense findings in the current study. The high background signal in the liver presents challenges for use of this agent in diseases with frequent liver metastases, and this aspect requires further study.

This study summarizes the radioligand kinetics of an RGD peptide in humans. The increase in SUV over time in tumors compared with the rapid clearance in blood and normal lung tissue (Fig. 4) is consistent with the selective high-affinity receptor binding in tumors and adequate pharmacokinetic properties. Primary and metastatic lesions showed radioligand uptake higher than that of the surrounding normal tissues ($P = 0.002$), with the exception of liver metastases, which were still detectable but with reversed contrast ($P = 0.0078$). Nonetheless, the absolute values of radioligand uptake in liver metastases (SUV_{BW} between 2 and 39 g/mL; Ki_{mod} between 2 and 69×10^{-5} mL of plasma/mL of tissue[s]) were high enough for clinical use (Table 2). The variable tumor uptake of the radioligand even in the same patient may be related to differences in angiogenesis; this finding needs further investigation. Kinetic modeling allowed quantitative assessment of radioligand–receptor interactions. The discernible linear phase in the Patlak plots implied a net-irreversible binding of radioligand to tumors within the imaging time. Ki_{mod} was less than Ki_{class}, suggesting that some of the ^{18}F-metabolites may have retained receptor-binding properties. Compartmental analysis of the data would help discern the magnitude of reversible- or irreversible-binding components within tissues, further elucidating the kinetics of tissue binding and specificity of the new tracer. With the net-irreversible trapping of the radioligand in tumors during the time examined, the residence time of ^{18}F-AH111585 was higher

in tumors than in adjacent normal tissues. Overall, the kinetics of ^{18}F-AH111585 support the choice of a late imaging time; for example, 40–60 min for future studies with the radioligand in breast cancer and possibly other tumors. For comparison, Beer et al. have recently reported the kinetics of ^{18}F-galacto-RGD in patients with squamous cell carcinoma of the head and neck (*29*). In their study, radioligand uptake peaked at 10–15 min, followed by a plateau phase or slight decrease over 60 min, and was associated with reversible kinetics (*29*).

^{18}F-AH111585 PET may have a role in imaging tumors and for monitoring antiangiogenic treatment. Xenografts derived from metastatic breast cancer bind to RGD peptide probes (*8,30,31*), supporting the use of ^{18}F-AH111585 for imaging metastatic breast cancer. A clinical proof-of-concept study in which radioligand uptake will be associated with $\alpha_v\beta_3$ receptor expression in tumors based on immunohistochemistry is also planned. It is hoped that this radioligand may help to support early clinical decisions regarding treatment response to antiangiogenic agents, including anti-VEGF, anti-VEGFR, and anti-$\alpha_v\beta_3$ receptor agents, because of the relationship between integrin expression and angiogenesis (*32*). In support of this hypothesis, a recent report showed a significant, 30%, decrease in ^{18}F-AH111585 PET uptake in tumors of drug-treated mice bearing Calu6 xenografts, compared with a 19% increase in control animals over the same time period when treated for 3 d with a pan-VEGFR inhibitor (*33*).

CONCLUSION

We suggest that ^{18}F-AH111585 PET is safe and can detect primary and metastatic breast cancer lesions. In addition, ^{18}F-AH111585 is only minimally metabolized *in vivo*

TABLE 2
Uptake and Kinetics of ^{18}F-AH111585 in Tumors and Normal Tissues

Patient no.	Tumor region	ROI (tissue type)	$SUV_{BSA} \times 10^{-3}$ (m²/mL)	SUV_{BW} (g/mL)	$Ki_{mod} \times 10^{-5}$ (mL plasma /mL tissue[s])	$Ki_{class} \times 10^{-5}$ (mL plasma /mL tissue[s])	FRT*	MRT
1	1	SCF	0.04	1.6	n/a	n/a	n/a	n/a
		Muscle	*0.02*	*1.0*	*n/a*	*n/a*	*n/a*	*n/a*
2	2	Breast tumor	0.05	2.1	3.8	4.4	0.46	840.4
		Normal breast	*0.02*	*0.6*	*1.6*	*1.7*	*0.26*	*1,381.1*
3	3	Liver met 1	0.09	3.5	9.4	9.9	0.11	1,005.8
	4	Liver met 2	0.10	3.9	11.8	10.0	0.14	286.8
	5	Liver met 3	0.08	3.1	9.4	9.6	0.26	1,216.6
	6	Liver met 4	0.089	3.4	10.2	10.5	0.32	950.8
	7	Liver met 5	0.04	1.4	3.7	3.9	0.08	361.9
	8	Liver met 6	0.09	3.5	9.7	10.0	0.14	585.8
		Normal liver	*0.11*	*4.5*	*9.8*	*10.8*	*0.05*	*91.5*
4	9	Liver met	0.08	3.4	3.7	4.4	0.05	170.9
		Normal liver	*0.10*	*4.6*	*4.7*	*5.8*	*0.01*	*194.3*
5	10	Lung met 1	0.96	36.0	68.8	72.7	0.17	47.9
	11	Lung met 2	0.07	2.6	2.3	3.0	0.04	226.5
	12	Lung met 3	0.05	2.0	4.0	4.2	0.15	714.3
	13	Lung met 4	1.07	40.0	72.5	78.1	0.19	2,227.2
		Normal lung	*0.02*	*0.9*	*1.0*	*1.3*	*0.05*	*333.5*
6	14	Lung met 1	0.18	6.8	27.5	28.7	0.25	2,415.3
	15	Lung met 2	0.17	6.2	21.8	23.8	0.23	2,032.6
	16	Lung met 3	0.18	6.6	24.6	26.5	0.23	615.5
	17a	Lung met 4a	0.14	5.2	22.1	21.1	0.26	2,761.2
	17b	**Lung met 4b**	**0.04**	**1.4**	**1.7**	**3.3**	**0.50**	**4,815.2**
	18a	Lung met 5a	0.14	5.2	17.4	19.2	0.32	1,458.2
	18b	**Lung met 5b**	**0.08**	**2.9**	**11.8**	**12.3**	**0.14**	**1,039.6**
		Normal lung	*0.03*	*1.0*	*2.4*	*3.0*	*0.10*	*450.7*
7	19	Liver met	0.09	3.5	7.4	10.0	0.04	172.7
		Normal liver	*0.10*	*3.7*	*6.9*	*9.4*	*0.04*	*195.9*

*FRT was calculated as ratio of unit impulse response function at 56.5 min to that at 1 min.

Data presented are analyses of radioligand uptake in 19 tumor regions from 18 CT-detectable lesions and 1 SCF. Whole or outer regions of tumor are indicated in standard font type, corresponding normal regions are in italics, and necrotic regions are in bold. In first patient, only SUV and area-under-curve calculations were performed because of concern about validity of ROI definition (not detected on CT). Met = metastasis; n/a = not applicable.

in humans, and activity is rapidly cleared from blood. Other than in the liver, the tissue-binding kinetics of ^{18}F-AH111585 in tumors, compared with normal tissues, are consistent with high-affinity receptor interaction. Tumor radioligand uptake largely varies among individuals and different tumor types, and even between tumors of the same type within 1 patient.

These findings have identified an objective time for receptor imaging in future studies of ^{18}F-AH111585 in breast and other cancers to assess its value in imaging tumors and for pharmacodynamic monitoring of antiangiogenic therapies.

REFERENCES

1. Hanahan D, Weinberg RA. The hallmarks of cancer. *Cell.* 2000;100:57–70.
2. Brooks PC. Role of integrins in angiogenesis. *Eur J Cancer.* 1996;32A:2423–2429.
3. Giancotti FG, Ruoslahti E. Integrin signaling. *Science.* 1999;285:1028–1032.
4. Albelda SM, Mette SA, Elder DE, et al. Integrin distribution in malignant melanoma: association of the beta 3 subunit with tumor progression. *Cancer Res.* 1990;50:6757–6764.
5. Bello L, Francolini M, Marthyn P, et al. Alpha(v)beta3 and alpha(v)beta5 integrin expression in glioma periphery. *Neurosurgery.* 2001;49:380–389.
6. Gasparini G, Brooks PC, Biganzoli E, et al. Vascular integrin alpha(v)beta3: a new prognostic indicator in breast cancer. *Clin Cancer Res.* 1998;4:2625–2634.
7. Sengupta S, Chattopadhyay N, Ray S, Mitra A, Dasgupta S, Chatterjee A. Role of aphavbeta3 integrin receptor in breast tumor. *J Exp Clin Cancer Res.* 2001;20:203–208.
8. Zitzmann S, Ehemann V, Schwab M. Arginine-glycine-aspartic acid (RGD)-peptide binds to both tumor and tumor endothelial cells in vivo. *Cancer Res.* 2002;62:5139–5143.
9. Beer AJ, Haubner R, Sarbia M, et al. Positron emission tomography using [18F]galacto-RGD identifies the level of integrin alpha(v)beta3 expression in man. *Clin Cancer Res.* 2006;12:3942–3949.
10. Haubner R, Weber WA, Beer AJ, et al. Noninvasive visualization of the activated alphavbeta3 integrin in cancer patients by positron emission tomography and [18F]galacto-RGD. *PLoS Med.* 2005;2:e70.

11. Koivunen E, Wang B, Ruoslahti E. Phage libraries displaying cyclic peptides with different ring sizes: ligand specificities of the RGD-directed integrins. *Biotechnology (NY).* 1995;13:265–270.

12. Indrevoll B, Kindberg GM, Solbakken M, et al. NC-100717: a versatile RGD peptide scaffold for angiogenesis imaging. *Bioorg Med Chem Lett.* 2006;16: 6190–6193.

13. Oken MM, Creech RH, Tormey DC, et al. Toxicity and response criteria of the Eastern Cooperative Oncology Group. *Am J Clin Oncol.* 1982;5:649–655.

14. Glaser M, Morrison M, Solbakken M, et al. Radiosynthesis and biodistribution of cyclic RGD peptides conjugated with novel ^{18}F-fluorinated aldehyde-containing prosthetic groups. *Bioconjug Chem.* Mar. 15, 2008 [Epub ahead of print].

15. Kenny LM, Vigushin DM, Al-Nahhas A, et al. Quantification of cellular proliferation in tumor and normal tissues of patients with breast cancer by [^{18}F]fluorothymidine-positron emission tomography imaging: evaluation of analytical methods. *Cancer Res.* 2005;65:10104–10112.

16. Mankoff DA, Shields AF, Graham MM, Link JM, Krohn KA. A graphical analysis method to estimate blood-to-tissue transfer constants for tracers with labeled metabolites. *J Nucl Med.* 1996;37:2049–2057.

17. Cunningham VJ, Jones T. Spectral analysis of dynamic PET studies. *J Cereb Blood Flow Metab.* 1993;13:15–23.

18. Beer AJ, Haubner R, Wolf I, et al. PET-based human dosimetry of ^{18}F-galacto-RGD, a new radiotracer for imaging alpha v beta3 expression. *J Nucl Med.* 2006; 47:763–769.

19. Haubner R, Wester HJ, Burkhart F, et al. Glycosylated RGD-containing peptides: tracer for tumor targeting and angiogenesis imaging with improved biokinetics. *J Nucl Med.* 2001;42:326–336.

20. Liu S, Hsieh W-Y, Jiang Y, et al. Evaluation of a ^{99m}Tc-labeled cyclic RGD tetramer for non-invasive imaging integrin $\alpha v \beta 3$-positive breast cancer. *Bioconjug Chem.* 2007;18:438–446.

21. Wester HJ, Kessler H. Molecular targeting with peptides or peptide-polymer conjugates: just a question of size? *J Nucl Med.* 2005;46:1940–1945.

22. Wu Y, Zhang X, Xiong Z, et al. microPET imaging of glioma integrin $\alpha v \beta 3$ expression using ^{64}Cu-labeled tetrameric RGD peptide. *J Nucl Med.* 2005;46:1707–1718.

23. Fox SB, Leek RD, Weekes MP, Whitehouse RM, Gatter KC, Harris AL. Quantitation and prognostic value of breast cancer angiogenesis: comparison of microvessel density, Chalkley count, and computer image analysis. *J Pathol.* 1995; 177:275–283.

24. Fox SB, Turner GD, Leek RD, Whitehouse RM, Gatter KC, Harris AL. The prognostic value of quantitative angiogenesis in breast cancer and role of adhesion molecule expression in tumor endothelium. *Breast Cancer Res Treat.* 1995;36:219–216.

25. Koukourakis MI, Giatromanolaki A, Sivridis E, Fezoulidis I. Cancer vascularization: implications in radiotherapy. *Int J Radiat Oncol Biol Phys.* 2000;48:545–553.

26. Weidner N, Folkman J, Pozza F, et al. Tumor angiogenesis: a new significant and independent prognostic indicator in early-stage breast cancer. *J Natl Cancer Inst.* 1992;84:1875–1887.

27. Cai W, Gambhir SS, Chen X. Multimodality tumor imaging targeting integrin $\alpha_v \beta_3$. *Bio Techniques.* 2005;39(suppl):S6–S17.

28. Stessels F, Van den Eynden G, Van der Auwera I, et al. Breast adenocarcinoma liver metastases, in contrast to colorectal cancer liver metastases, display a non-angiogenic growth pattern that preserves the stroma and lacks hypoxia. *Br J Cancer.* 2004;90:1429–1436.

29. Beer AJ, Grosu AL, Carlsen J, et al. [^{18}F]galacto-RGD positron emission tomography for imaging of $\alpha v \beta 3$ expression on the neovasculature in patients with squamous cell carcinoma of the head and neck. *Clin Cancer Res.* 2007; 13:6610–6616.

30. Pasqualini R, Koivunen E, Ruoslahti E. Alpha v integrins as receptors for tumor targeting by circulating ligands. *Nat Biotechnol.* 1997;15:542–546.

31. Pécheur I, Peyruchaud O, Serre CM, et al. Integrin alpha(v)beta3 expression confers on tumor cells a greater propensity to metastasize to bone. *FASEB J.* 2002;16:1266–1268.

32. Miller JC, Pien HH, Sahani D, Sorensen AG, Thrall JH. Imaging angiogenesis: applications and potential for drug development. *J Natl Cancer Inst.* 2005;97:172–187.

33. Morrison M, Ricketts S, Barnett J, Constantinou M, Tessier J, Wedge SR. Monitoring tumor response to ZD4190 therapy with an ^{18}F labeled angiogenesis imaging agent. 2007 ASCO Annual Meeting Proceedings. *J Clin Oncol.* 2007; 25:10507.